GFZ

Helmholtz-Zentrum
POTSDAM

The upper mantle under Central Europe: indications for the Eifel plume

Steffen Grunewald,[1] Michael Weber,[1,2] and Rainer Kind[1,3]

[1] *GeoForschungsZentrum, Telegrafenberg, 14473 Potsdam, Germany. E-mail: steffen@gfz-potsdam.de*
[2] *Institut für Geowissenschaften, Universität Potsdam, Karl-Liebknecht-Strasse 24/H25, 14476 Golm, Germany*
[3] *Fachbereich Geowissenschaften, Freie Universität, Malteserstrasse 88-100, 12249 Berlin, Germany*

SUMMARY

The topographies of the upper mantle discontinuities at 410 and 660 km depth under Central Europe have been mapped. Using a modified receiver function approach, we processed data recorded at selected Central European broad-band stations during the years 1981–1998. Below the Rhenish massif near the Eifel region we identified a significantly deepened 410 discontinuity that may have its origin in an upgoing mantle plume, in agreement with recently derived results from seismic tomography. We have furthermore found evidence for a northward-dipping structure at the lower boundary of the mantle transition zone below the Alps, possibly related to the subduction that occurred during the closing of the Tethys.

Key words: mantle discontinuities, plumes, receiver functions, upper mantle.

1 INTRODUCTION

At regional scale, there are few investigations of the structure of the lithosphere and upper mantle covering the area of Central Europe. This area is of particular interest to geodynamic research since it contains the European Cenozoic Rift System with the Rhine Graben and the volcanic fields of the Eifel, for example. This paper focuses on imaging the structure of the upper mantle under Central Europe and on creating maps of the major upper mantle discontinuities.

An important topic of recent geophysical research is mantle plumes, the understanding of which heavily influences our knowledge of material and heat-flow processes taking place in the mantle as a whole. Recent work by Li *et al.* (1999) on the Hawaii plume showed that even narrow structures (of the order of 100 km) can be imaged by seismological methods. The proposed plume beneath the Eifel volcanic region (Budweg *et al.* 1999; Ritter *et al.* 2001), which may be the manifestation of an anomaly located in the lower mantle under Central Europe (Goes *et al.* 1999), is one target of this investigation.

Like seismic tomography, *S*-wave splitting and long-range refraction seismic profiles, receiver functions (Vinnik 1977; Langston 1979; Ammon 1997) are widely used to image and characterize structures and special features of the Earth's crust and upper mantle. The receiver function (RF) method uses three-component recordings to reconstruct the Earth's response in a source- and receiver-independent way. The *S* waves created by conversions at velocity and density contrasts along the travel path of the primary *P* wave are separated, and the conversion operator—the 'receiver function'—is obtained by deconvolving the *P* signal from its conversion products.

In this study, special attention has been given to improving several steps of the receiver function method, for example, minimizing the influence of crustal inhomogeneities and Moho depth, which contribute to receiver-dependent mislocations and intracrustal traveltime variations. In addition, we have developed a new imaging procedure that takes into account the wave character of seismic signal propagation by distributing conversion amplitudes over Fresnel zones.

2 PROCESSING OF THE BROAD-BAND DATA SET

The source of the data used in this study is the German Regional Seismic Network (GRSN) together with its predecessor, the Gräfenberg array (GRF, operated by the German Bundesanstalt für Geowissenschaften und Rohstoffe, recording from 1976). To expand the area covered by receiver stations, the station WLF (Walferdange, Luxembourg), part of the GEOFON network (operated by the GeoForschungsZentrum Potsdam) has been added (Fig. 1).

Out of 18 years of continuous broad-band recordings of up to 19 simultaneously working stations, a total of 1133 events from an epicentral distance range 30°–95° with m_b magnitudes of at least 5.8 have been selected (Fig. 2), resulting in approximately 8500 three-component seismograms with 20 samples s^{-1} sampling rate. During a visual check of all waveforms, incomplete and distorted data as well as noisy recordings were eliminated.

The choice of an inappropriate filter can heavily influence the information contained in the recorded data. Since the recorded signals have to be assumed to be mixed-phase, the processing of the data avoids pre-filtering of the data.
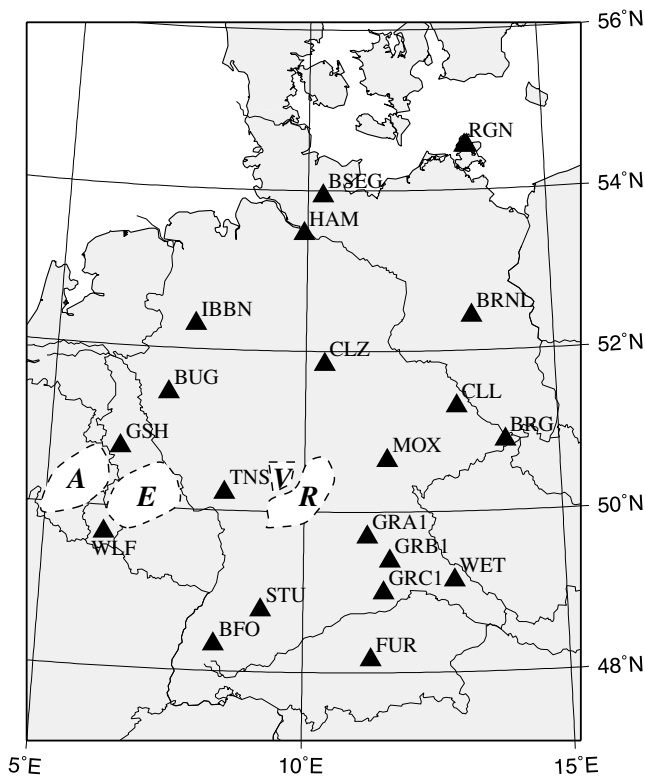
Figure 1. Locations of the stations used. A, E, R and V denote the Ardennes, the Eifel, the Rhön mountains and the Vogelsberg, respectively.

2.1 Rotation

The first step in the data processing is the separation of the *P* wave from near-surface conversions (from the Moho as well as from intracrustal contrasts). The *P* wave is assumed to be polarized along the ray path, and *SV* waves should be polarized perpendicular to *P*. Thus it is best to perform a rotation of

Figure 2. Azimuthally equidistant map of events used ($m_b \geq 5.8$).

the three-component seismograms into another orthogonal coordinate system related to the directions of particle motion. In this ray-centred coordinate system, all the energy of the initial *P* wave would, in the absence of shear wave anisotropy, be concentrated on the longitudinal (*L*) component, and *P*-to-*S* conversions would contribute only to the *Q* component, which lies in the great-circle plane.

Crustal inhomogeneities such as low-velocity wedges (Krüger & Weber 1992) and a dipping Mohorovičić; discontinuity (Gossler *et al.* 1999) produce significant deviations of the particle motion from the theoretical values. These deviations from the theoretical rotation angles introduce noticeable errors. Therefore, the correct rotation angles were determined from the data themselves. Since noise is a significant problem on the horizontal components, the traditional way of finding the major axis of particle motion via polarization analysis was not successful for most seismograms, even after low-pass filtering (e.g. fourth-order Butterworth filter with a corner frequency of 0.2 Hz).

Therefore, another method, similar to the processing applied in reflection seismic exploration and known as vertical stacking, was used. Events from a selected backazimuth interval (sliding window of $\pm 15°$ size, in 1° steps) were grouped together. Due to the irregular distribution of seismically active regions, the resulting groups contain different numbers of events (*cf.* Fig. 2). For the directions to the major earthquake source areas there are several hundred events, while in southern directions there are only very few data available.

For these event groups the total *P*-wave potential energy on the transverse component was minimized relative to the radial component, thus minimizing the ratio of transverse to overall energy (Grunewald 2000):

$$\sum_{\text{all events}} \left(\sum u_n^{T\,2} \Big/ \sum u_n^{R\,2} \right) \rightarrow \min ,$$

where u^T and u^R denote the transverse and radial signal components, respectively. Varying the backazimuth interval from 0° to 360° using a sliding window, a smoothed dependence of the rotational angle correction on the backazimuth was determined. Typical azimuthal corrections are of the order of 5°–10°. For the determination of the angle of incidence, the sliding-window technique showed no advantage over the faster individual polarization analysis approach, therefore the latter was used.

The rotation corrections for the GRF station GRA1 are shown in Fig. 3. Comparison with earlier work by Krüger & Weber (1992) shows good agreement with the mislocation vectors of the Gräfenberg array stations.

2.2 Deconvolution

To make the recordings from different earthquakes gathered at one receiver point comparable, one has to take into account the fact that the source time functions vary widely. Thus the separation of the conversions from the primary *P*-wave is done by deconvolution. Two major ways to perform this operation are possible: spectral division and spike deconvolution (e.g. Buttkus 1991). The inverse procedure to folding, which corresponds to multiplication of spectra in the frequency domain, would be a division of signal spectra. In practice, with discrete digitized signals, problems can occur. Since small values in the denominator would cause the result to be unstable, white noise
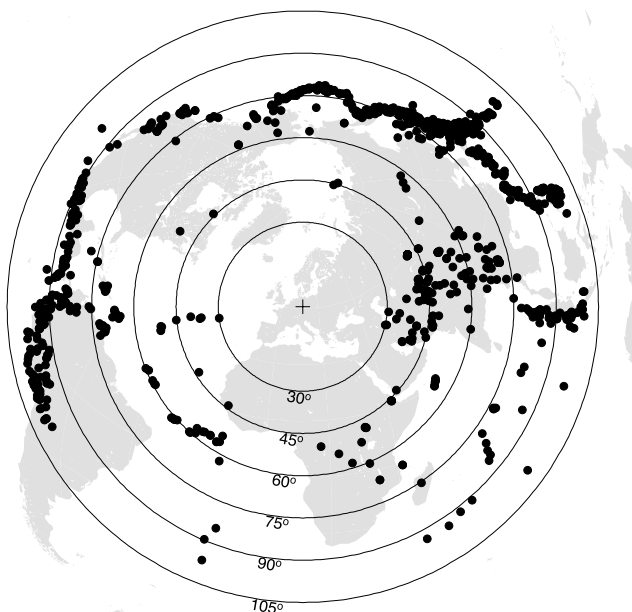
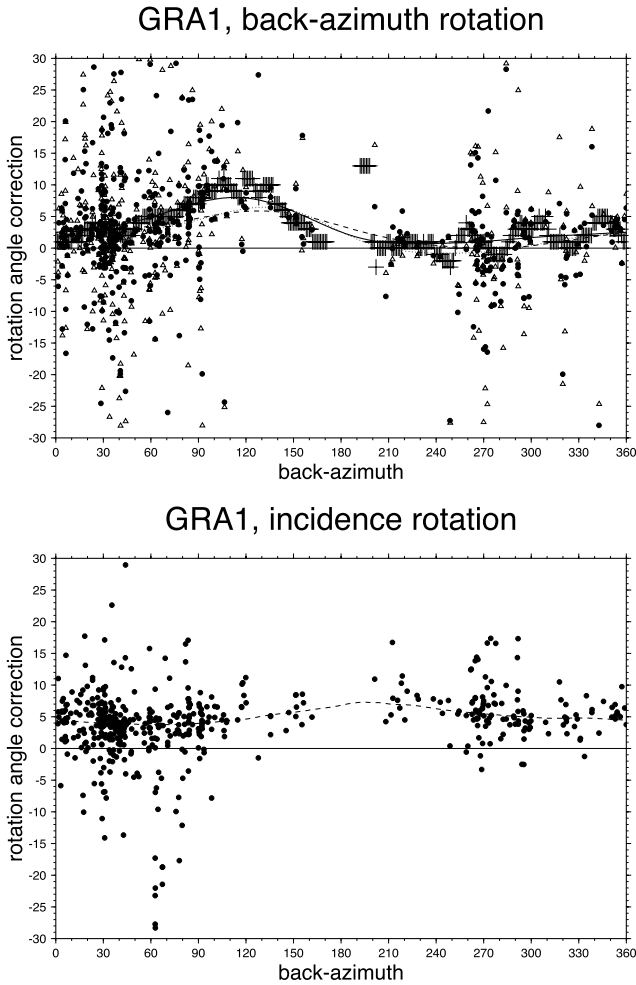## GRA1, back-azimuth rotation

GRA1, incidence rotation

Figure 3. Correction for horizontal (backazimuth, top) and vertical (incidence, bottom) rotation. Full circles/dashed line: values derived from polarization analysis. Open triangles/dotted line: same after 5 s low-pass filtering. Crosses/solid line: cluster energy minimization, sliding-window technique with constant increment of 1°.

is added to the spectrum or gaps are filled up to a certain water level. The parameters of this spectral pre-whitening have to be chosen carefully and on a per-event basis, usually by trial and error. To achieve a consistent treatment of all data, the spike deconvolution, which uses a generalized Wiener optimum filter approximating the inverse of the *P* signal, was used. Wiener's approach consists of the construction of a digital approximation of the inverse of the time-series that, if folded onto the original time-series, produces a bandpass-limited delta pulse. Of course it is desirable to achieve a narrow pulse. This method allows non-causal filter operators to be produced, so the time delay of the delta pulse would be zero. This approach is better suited for mass-data processing since the results are less sensitive to process parametrization.

2.3 Moveout correction

Since waves from different epicentral distances arrive at the receiver at varying incidence angles, the representation of the conversion operators (receiver functions) in the time domain has to be corrected for these different distances. This procedure is known in reflection seismics as moveout correction (Yilmaz

1987; Yuan *et al.* 1997). This process maps each segment of the actual ray path onto the corresponding piece of a reference path. While seismologists usually correct to the mean distance and slowness, the reflection seismic approach uses slowness 0 or, in other words, rays arriving from directly below the receiver (vertical incidence, Fig. 4). In the latter case the correspondence of traveltime to depth is easily computed from a velocity model.

Fig. 5 shows the theoretical piercing points of rays, computed by ray tracing using the IASP91 earth model (Kennett 1991; Kennett & Engdahl 1991) for the selected events recorded at the corresponding stations, for conversion depths at 35, 210, 410 and 660 km. Also shown are the isochrons corresponding to signal periods of 1, 2, 5 and 10 s respectively. The dominant period of the data is in the 3–5 s range, so a λ/4 Fresnel zone coincides roughly with the 1 s isochron.

While the coverage and the overlapping pattern of neighbouring stations are poor for shallow conversions, a good coverage at depths below 300 km is achieved. See Appendix B for a short discussion of coverage and reliability.

To give an impression of the data quality, all records whose theoretical 410 km conversion points would fall in a 1° wide strip in the N–S direction along the 13°E meridian were selected and plotted in north-to-south order (Fig. 6). The image shows conversions from the base of the sediment layer (first 2 s) and from Moho level (about 5 s) and the mantle discontinuities at about 410 and 660 km for both the raw and the low-pass filtered data. Particularly evident is the remarkable influence of shallow structures on the *P–S* traveltime delays. Thus to map traveltimes reliably into depth, station-dependent crustal models must be used. Otherwise, time differences of up to about 1 s would be mapped into depth and interpreted as about 10 km of topography on the conversion horizons in the upper mantle.

2.4 Crustal corrections

To obtain 1-D crustal models, two methods were used. First an inversion of crustal receiver functions was used, following the approach of Kind *et al.* (1995), which led to complex crustal models beneath some of the network stations but was in general agreement with the Moho depth values obtained by
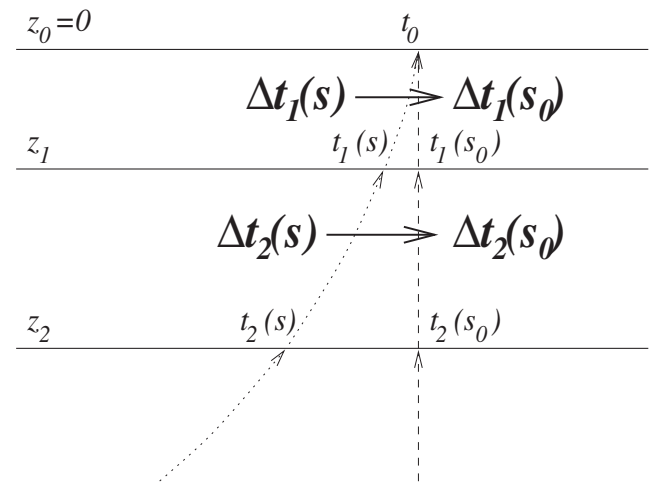

Figure 4. Moveout correction to vertical incidence. Each interval of traveltime difference is mapped onto its equivalent for a ray path perpendicular to the surface.
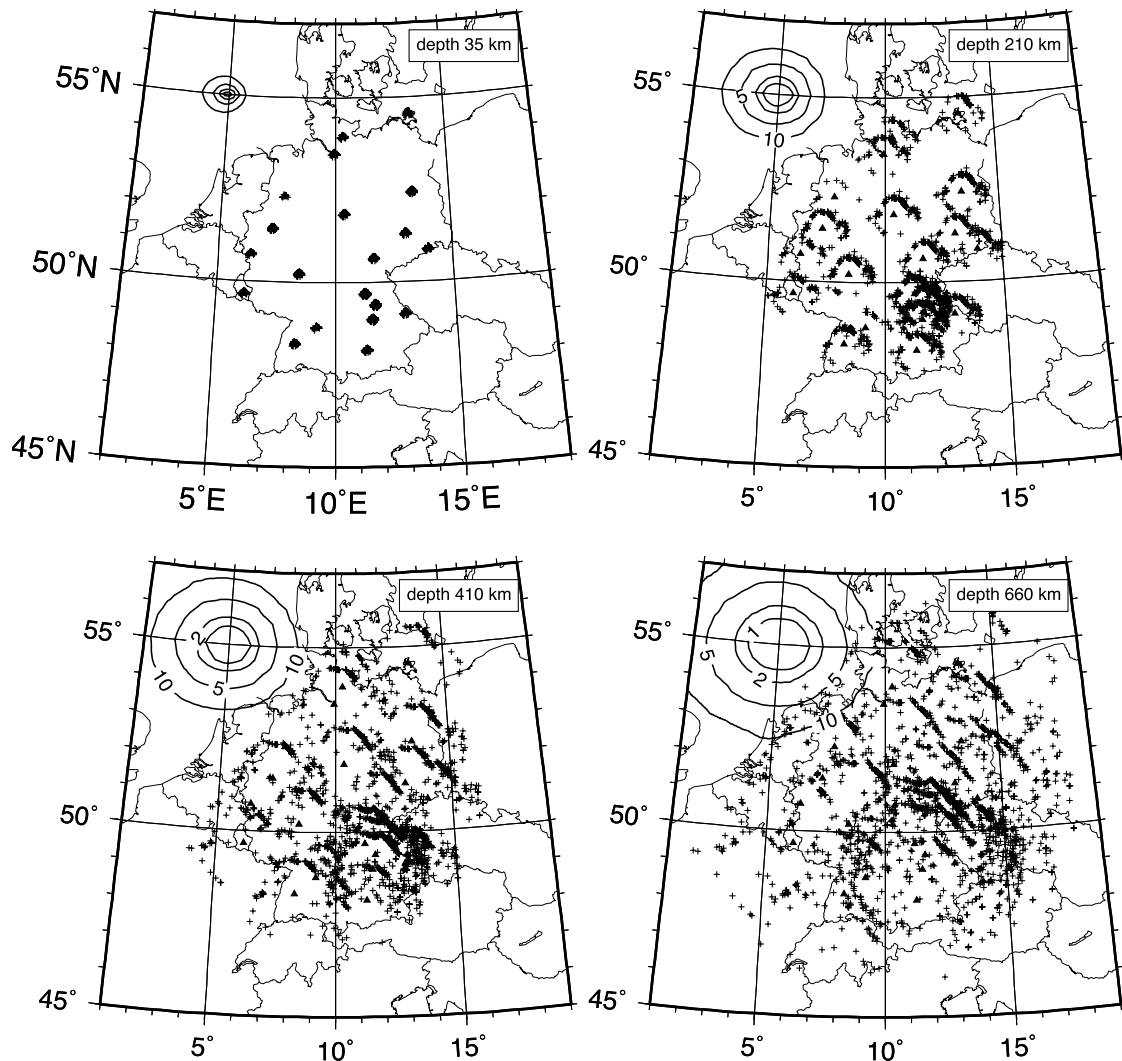
Figure 5. Locations of piercing points through discontinuities at 35 km (Moho), 210 km (Lehmann), 410 km and 660 km depth (mantle transition zone). Also shown are the corresponding Fresnel zones for wave periods of 1, 2, 5 and 10 s.

the European Geotraverse EGT (Blundell *et al.* 1992). For an additional check, the procedure of Zhu & Kanamori (2000), who perform a 2-D grid search in the v_P/v_S–depth plane to find the most probable parameters of a mean crust was expanded to a 3-D grid search, parametrized by crustal thickness z, mean v_P and v_P/v_S ratio. Unfortunately, this method is very insensitive to the v_P/v_S ratio. Modifying the approach of Zhu & Kanamori (2000), the EGT Moho depth (Blundell *et al.* 1992) was chosen as a fixed input since it is more robust. Both methods resulted in similar crustal models. For each station this crustal model replaced the top layers of the global model IASP91. These station-dependent models were then used as the base for the following pre-stack migration. (See Appendix A for the individual crustal models derived.)

3 RESULTS

Starting with a process developed by Yuan *et al.* (1997), who applied a migration technique from exploration seismics, the individual receiver function time-series were mapped along their corresponding ray paths into 3-D space using the station-specific velocity models (see Appendix A). The time-discrete

receiver functions were transformed into conversion amplitude values populating a 3-D grid of volume elements [voxels of 10 km × 10 km horizontally × 2 km vertically, *cf.* Kidd (1999), Fig. 7]. The contributions to each voxel were then stacked to reduce noise.

Due to the wave nature of the elastic deformation, spatial smearing of wave energy that finds its expression in the Fresnel zones (Fig. 5) was taken into account. This was achieved by distributing the RF amplitudes over Fresnel zones using a Gaussian distribution (with a $1/e$ decay at the 1 s isochron). This means that each single receiver function contributes to several voxels per depth slice. The resulting 3-D grid volume was then used as a starting point for selecting slices horizontally or vertically.

Figs 8 and 9 show several depth slices, each 2 km thick, near the major upper mantle discontinuities. Positive conversion coefficients are expected at discontinuities separating larger elastic velocities and densities below from smaller ones above. The sections at 410 and 660 km depth are dominated by orange-red colour indicating a weak variation of discontinuity topography at the expected depths. Two features are most significant: (1) the large blue dot at 410 km depth northeast
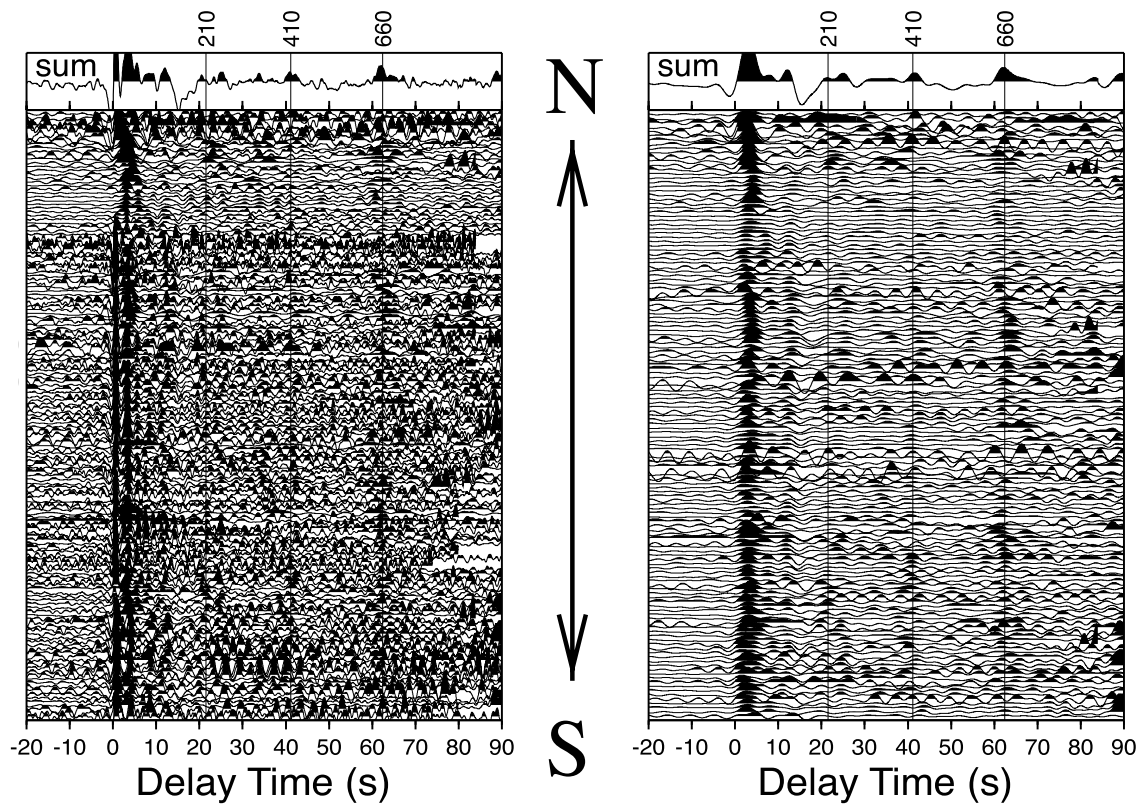
Figure 6. Moveout-corrected receiver functions (*P–S* delay times) collected in the meridian strip $13\pm0.5°$E, sorted north to south (from top to bottom). Left: unfiltered (raw) data; right: data after low-pass filtering (5 s). The peaks in the interval ≈ 2–15 s denote conversions at the sediment base and the Moho, followed by crustal multiples. Also shown are the theoretical IASP91 conversion delays of the 210, 410 and 660 km discontinuities.

of BUG (at about 52°N/8°E), which is an expression of a subcrustal anomaly whose origin is still unclear, and (2) the east–west belt of high conversion amplitudes dropping below 430 km depth beneath the Ardennes–Eifel–Rhön/Vogelsberg area (see Fig. 1).
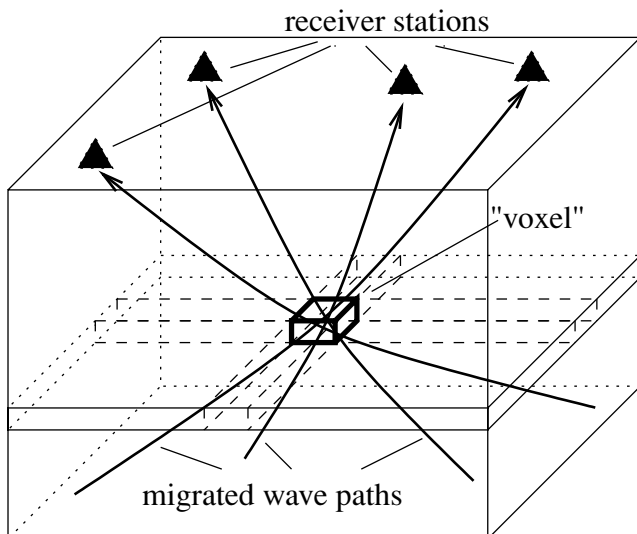

Figure 7. Pre-stack migration. The individual receiver functions in the time domain are converted into the space domain and discretized into volume elements (voxels). The contributions from all rays to each voxel can then be summed.

In order to visualize the topography of the discontinuities better, we performed a grid search over a depth interval including the typical depth of the discontinuity. By calculating the weighted average of positive conversion amplitudes in a 50 km × 50 km × 2 km grid, we obtained 'effective conversion depth' values (Figs 10 and 11). A comparison of the results derived from raw broad-band data with those obtained using low-pass (Butterworth 5 s) filtered data shows good agreement. The striking features of Figs 10 and 11 are the considerable deepening of the 410 km discontinuity along an east–west line at 51°N in the western part of the investigated area on the one hand and the flat topography of the 660 km discontinuity on the other.

To understand better the dynamics in the area showing the 410 depression, which is closely related to Tertiary and Quaternary volcanism, in particular with the expected Eifel plume in mind, we now describe vertical cross-sections through the data volume.

Fig. 12 shows S–N and W–E sections 0.1° wide intersecting at 50.1°N/6.9°E, which coincides with the centre of the Eifel Plume Project's station pattern (Ritter *et al.* 1998; Budweg *et al.* 1999). A large 'blob' of high conversion amplitude is dominant at the crossing-point of the profiles, indicating a 410 km discontinuity lowered by at least 20 km and/or a strong negative anomaly of at least the shear wave velocity in the layer(s) above. Ritter *et al.* (2000a, 2001), by applying tomographic methods, found a v_P anomaly 100 km wide below the recent volcanic fields of the order of 1–2 per cent. A temperature variation of about 150–200 K would produce such an anomaly
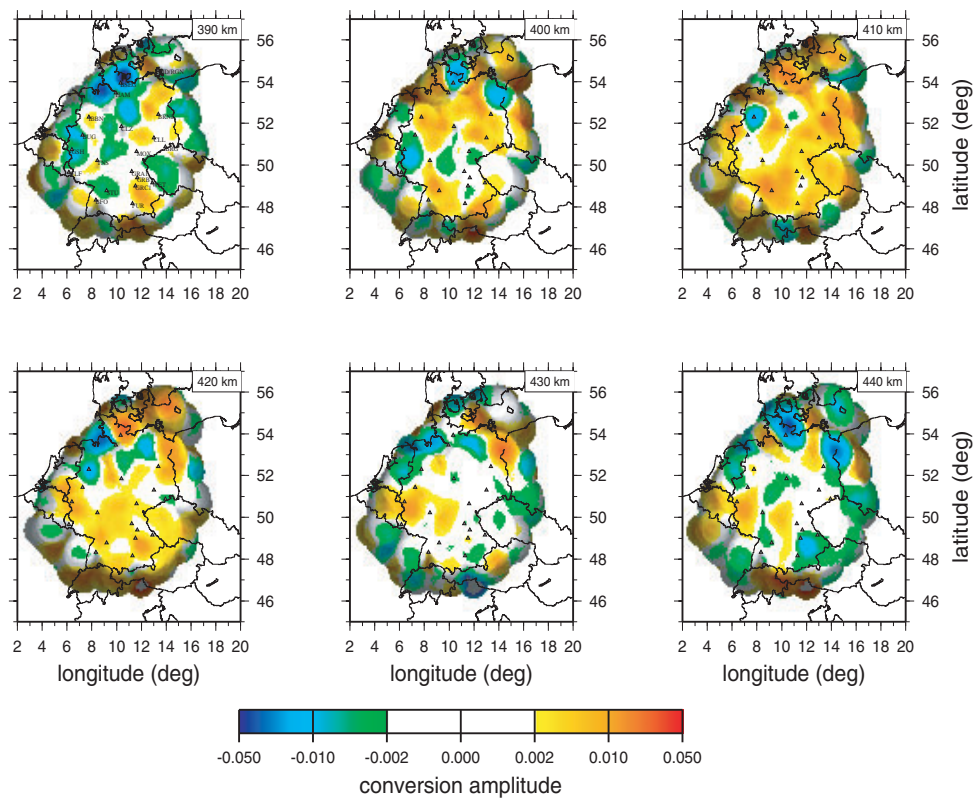
Figure 8. Horizontal sections through the 3-D data volume from 390 to 440 km depth. The locations of the stations are shown as black triangles. The RF signal amplitude has been encoded into the colour value, while the signal quality (coverage) is indicated by an intensity contrast. See Fig. 1 for areas of interest such as the Eifel region.
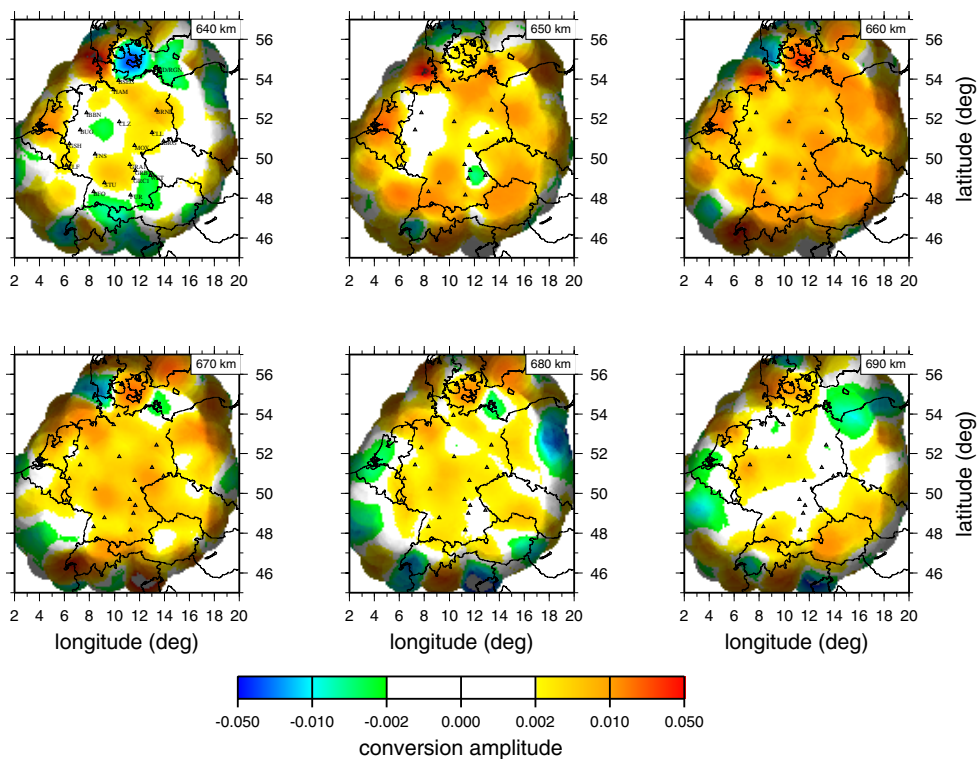

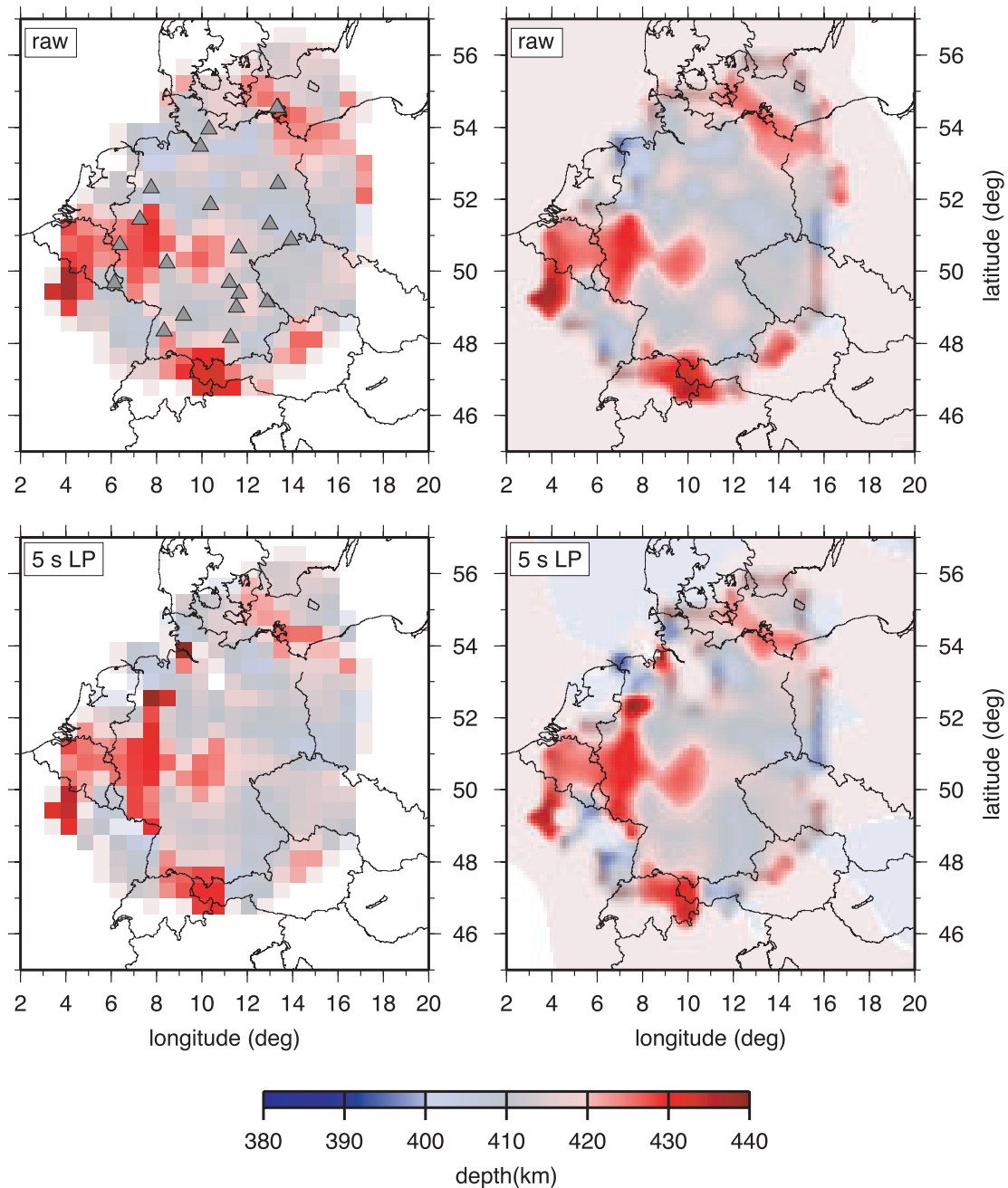**Figure 9.** As Fig. 8 for the 640–690 km depth range.

Figure 10. Left: effective conversion depth obtained for the depth range from 400 to 440 km, averaged over 50 km × 50 km cells. The colour scale has been chosen to emphasize larger deviations from the mean values. Right: the same after applying a horizontal low-pass smoothing. Top: results of processing raw broad-band data. Bottom: results after low-pass (5 s) filtering the input data.

and could partly explain both the deepening of the discontinuity due to the positive Clapeyron slope of the $\alpha \rightarrow \beta$ transition in the olivine system and the reduced shear wave velocities.

At this point it is necessary to point out that structures significantly smaller than 150 km laterally cannot be resolved by the receiver function method. The 1 s isochrons at 410 km depth have a diameter of comparable size (200 km, Fig. 5). Moreover, the ray paths corresponding to initial *P* and converted *S* waves at the same surface point are about 100 km apart at 410 km depth. Therefore, both wave types would probe different features of the mantle. Thus the broadening of

the conversion maximum between 410 and 440 km depth could be due to waves passing only partially through the anomalous mantle zone.

If the plume in the upper mantle under the Eifel were connected to a deep root in the lower mantle, an updoming of the 660 km discontinuity would be expected due to the negative Clapeyron slope for the γ-spinel$\rightarrow$magnesiowüstite$+$perovskite transition. No indication for such a feature is visible, arguing against a thermal anomaly at the bottom of the transition zone. Preliminary results of Budweg *et al.* (2000) confirm this result.
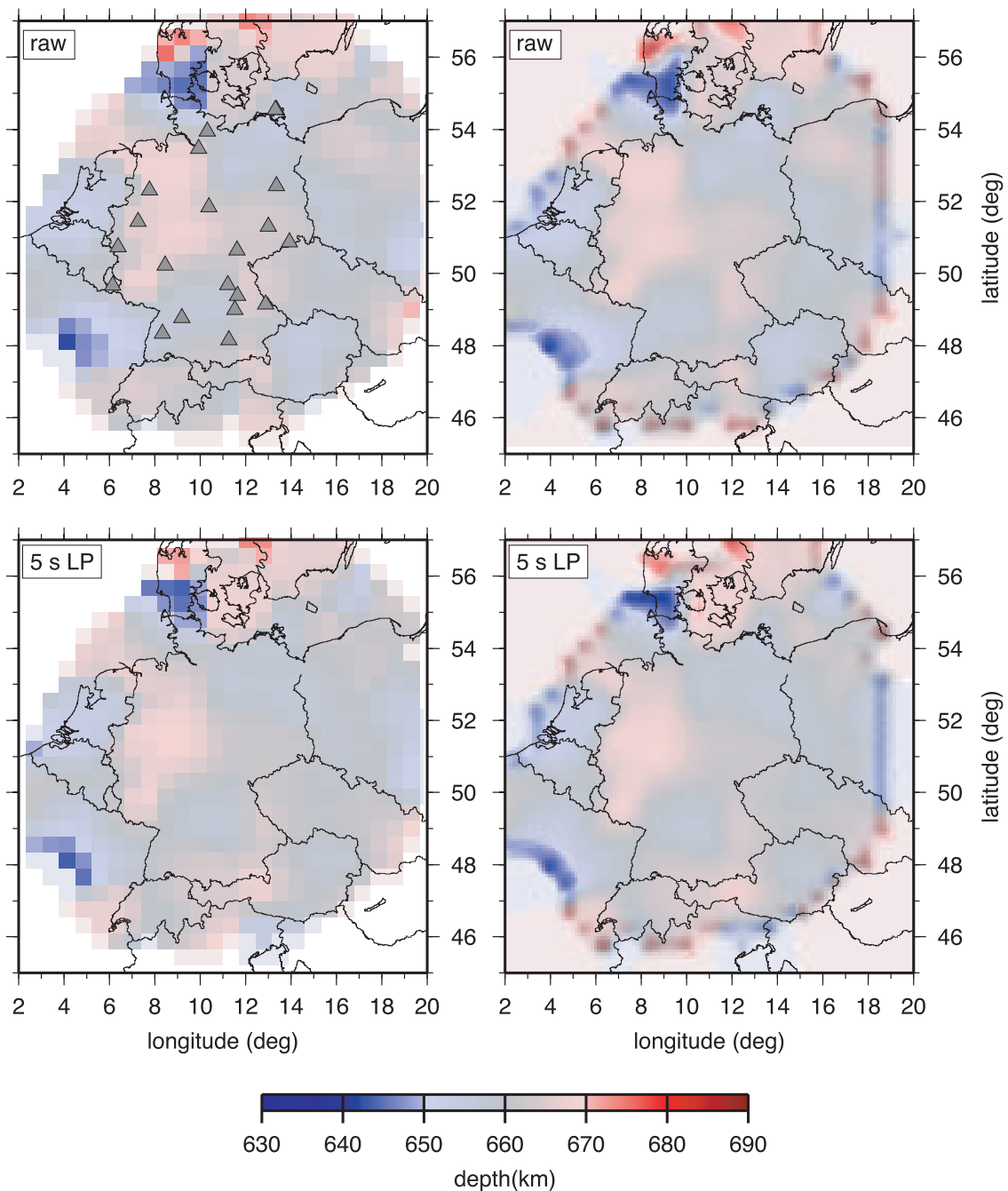
Figure 11. Same as Fig. 10 for the depth range 640–680 km.

In principle, these findings are in agreement with the tomographic results of Goes *et al.* (1999), which show a low-velocity anomaly in the lower mantle feeding small-scale upper mantle upwellings. Under Central Europe the transfer of heat, which may very well be one of the principal causes of the velocity anomalies, might be influenced or even cut off by a subducting slab-like structure, which clearly shows up in their tomographic image as a high-velocity layer. This slab-like

feature has already been imaged by Spakman *et al.* (1993), who, in a vertical section along 10°E (their Fig. B9), recognized a northward-dipping slab fragment. However the authors gave no explanation of its origin. Below we discuss the geodynamic setting of this feature.

To image this slab in our data volume in more detail, all data from 4° wide meridian strips were stacked, amplifying signals that are coherent in the east–west direction (Fig. 13). The
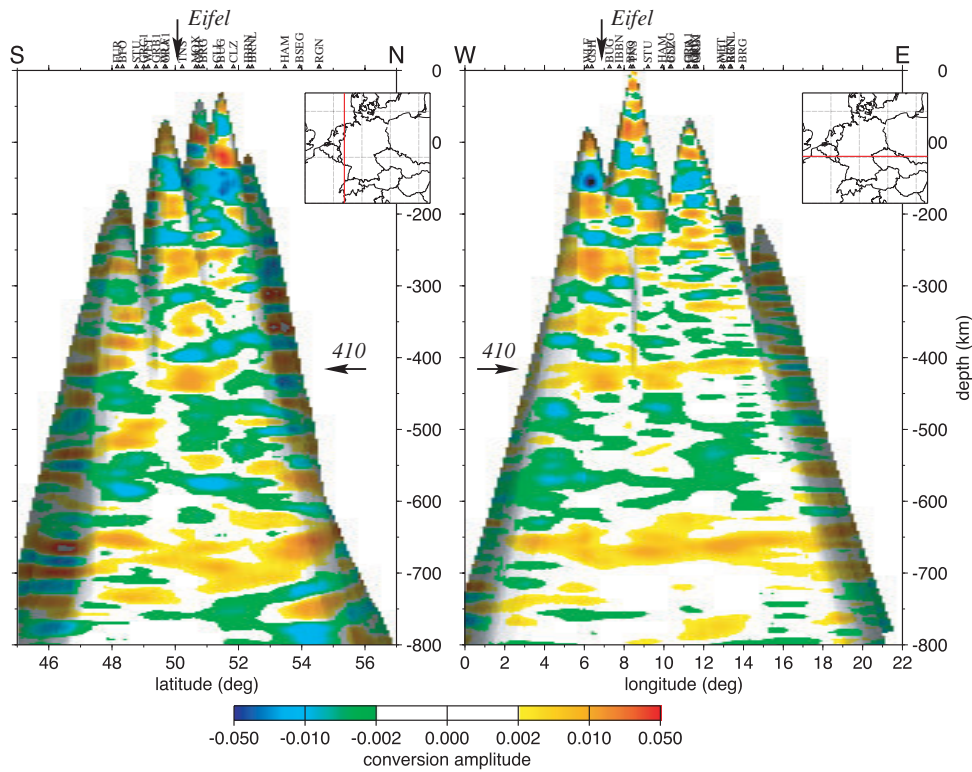
Figure 12. Vertical sections through the Eifel region (at 50.1°N, 6.9°E, slice thickness 10 km). Insets show the locations of the sections. Left: north–south slice; right: west–east slice. (Note the vertical exaggeration of 1:2.5.)

western stack (Fig. 13, left) shows weak but consistent signatures of a P–S conversion horizon starting at the lower boundary of the transition zone in the southern part of the area covered. It is located near the Alps, which south of Germany also trend mainly E–W. It dips at about 11°N, which is about the same angle that can be read off the vertical section of Spakman *et al.* (1993).
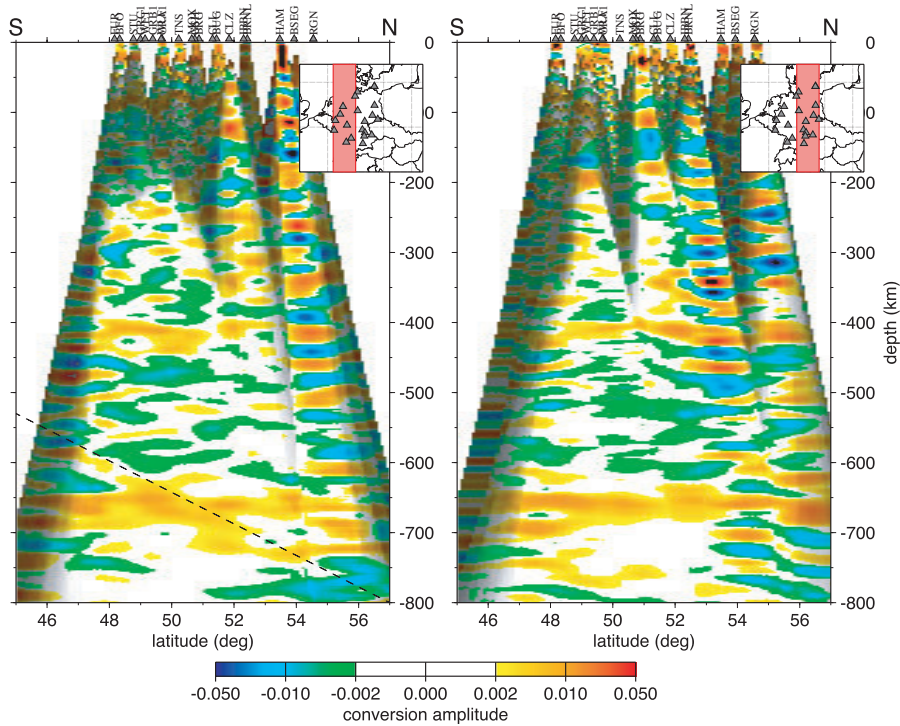

Figure 13. North–south sections along the meridian strips 6–10°E and 10–14°E. The red lines from north to south in the insets show the locations of the corresponding strips. The dashed line in the left part indicates the slab fragment dipping northwards. (Note the vertical exaggeration of 1:2.5.)

If the pattern of conversions below 550 km depth in the left part of Fig. 13 is associated with a slab fragment, this would be the first time that a slab could be identified by receiver function analysis at such a large depth.

4 DISCUSSION

Despite the limited spatial resolution of receiver functions in the upper mantle, we were able to detect a 150 km wide and 20 km deep depression of the 410 km discontinuity in the upper mantle under the Eifel region. This is indicative of a zone of increased (by about 200 K) temperature. This finding agrees with the reduced *P*-wave velocity detected by tomographic analysis (Ritter *et al.* 2001) down to about 430 km depth beneath the central region of the Eifel volcanic fields. Of course, the receiver function method cannot separate the effect of increased temperature from that of reduced seismic velocities, but one should expect that both effects contribute to the anomalous depth of the 410 km discontinuity found in this study.

Other investigations (Goes *et al.* 1999; Budweg *et al.* 2000) provide additional evidence that this discontinuity anomaly might in fact be the result of a plume generated in the lower mantle. The bottom of the transition zone at about 660 km depth does not seem to be affected by this plume. A possible explanation of this observation of an unperturbed 660 km discontinuity is that a cold slab fragment separated the hot zone in the upper mantle from its heat source at larger depths (Spakman *et al.* 1993; Goes *et al.* 1999).

With the stations available, we cannot track this hypothetical slab fragment outside the area covered here. A possible origin of this slab is the closing of the Tethys ocean (Stampfli *et al.* 1998). While this hypothesis needs further investigation, it is supported by the approximate E–W trend of the Alpine collisional belt, which is parallel to the region of anomalous effective depth for the 410 km discontinuity.

Geodynamic problems and questions in connection with the features identified by this study are as follows.

(i) The origin of the hypothetical slab fragment and the corresponding timescale have to be determined. Of particular interest is the position and size of the slab at the time of closure of the Tethys ocean (35 Myr ago) and its interaction with the volcanism in the Vogelsberg area.

(ii) If the upper mantle was separated from the lower mantle heat source, when did this happen?

(iii) Additional investigation of the slab itself should be performed. Due to the way the processing was carried out, we cannot give an absolute value for the conversion amplitude of this slab.

Further geodynamic, geochemical and geophysical investigations by the Eifel Plume and Transalp working groups are underway to gain additional information about some of these features.

REFERENCES

Ammon, C.J., 1997. *An Overview of Receiver Function Analysis,* http://www.eas.slu.edu/People/CJAmmon/HTML/RftnDocs/rftn01.html, Saint Louis University, St. Louis, MO.

Blundell, B., Freeman, R. & Mueller, St. (eds), 1992. *A Continent Revealed. The European Geotraverse,* Cambridge University Press, Cambridge.

Budweg, M., *et al.*, 1999. A 400 km long broadband antenna in the Eifel Region, *Observatories and Research Facilities for European Seismology,* ORFEUS Newsletter, Vol. 1, No. 3, http://orfeus.knmi.nl/.

Budweg, M., *et al.*, 2000. The upper mantle in the region of the Eifel, *AGU Fall Mtng.* S22B-07, in: *EOS, Trans. Am. Geoph. Un.,* **81,** No. 48, F926.

Buttkus, B., 1991. *Spektralanalyse und Filtertheorie in der angewandten Geophysik,* Springer, Berlin.

Goes, S., Spakman, W. & Bijward, H., 1999. A lower mantle source for central European volcanism, *Science,* **286,** 1928–1931.

Gossler, J., *et al.*, 1999. Major crustal features between the Harz Mountains and the Baltic Shield derived from receiver functions, *Tectonophysics,* **314,** 321–333.

Grunewald, S., 2000. Untersuchungen zur regionalen Struktur von Lithosphäre und oberem Erdmantel unter Zentraleuropa mittels konvertierter seismischer Phasen, *PhD thesis,* University of Potsdam, Germany.

Kennett, B.L.N. (ed.), 1991. *IASPEI 1991 Seismological Tables,* Research School of Earth Sciences, Australian National University, Canberra.

Kennett, B.L.N. & Engdahl, E.R., 1991. Traveltimes for global earthquake location and phase identification, *Geophys. J. Int.,* **105,** 429–465.

Kidd, G.D., 1999. Fundamentals of 3-D seismic volume visualization, *The Leading Edge,* **18,** 702–712.

Kind, R., Kosarev, G.L. & Petersen, N.V., 1995. Receiver functions at the stations of the German Regional Seismic Network, *Geophys. J. Int.,* **121,** 191–202.

Krüger, F. & Weber, M., 1992. The effect of low-velocity sediments on the mislocation vectors of the GRF array, *Geophys. J. Int.,* **108,** 387–393.

Langston, C.A., 1979. Structure under Mount Rainier, Washington, inferred from teleseismic body waves, *J. geophys. Res.,* **84,** 4749–4762.

Li, X., Kind, R., Priestley, K., Sobolev, S.V., Tilmann, F., Yuan, X. & Weber, M., 1999. Mapping the Hawaii plume conduit with converted seismic waves, *Nature,* **405,** 938–941.

Ritter, J.R.R., Christensen, U., Achauer, U., Bahr, K. & Weber, M., 1998. Search for a mantle plume under Central Europe, *EOS, Trans. Am. geophys. Un.,* **79,** 420.

Ritter, J.R.R., *et al.*, 2000. The teleseismic tomography experiment in the Eifel region, Central Europe: design and first results, *Seism. Res. Lett.,* **71,** 437–443.

Ritter, J.R.R., Jordan, M., Christensen, U.R. & Achauer, U., 2001. A mantle plume below the Eifel volcanic fields, Germany, *Earth planet. Sci. Lett.,* **186,** 7–14.

Spakman, W., van der Lee, S. & van der Hilst, R., 1993. Traveltime tomography of the European-Mediterranean mantle down to 1400 km, *Phys. Earth planet. Inter.,* **79,** 3–74.

Stampfli, G.M., *et al.*, 1998. *Geodynamic Evolution of the Alpine Tethys,* http://www-sst.unil.ch/research/plate_tecto/alp_tet.htm, University of Lausanne.

Vinnik, L.P., 1977. Detection of waves converted from P to SV in the mantle, *Phys. Earth planet. Inter.,* **15,** 39–45.

Yilmaz, O., 1987. Seismic data processing, *SEG Investigations in Geophysics,* No. 2, SEG, Tulsa, OK.

Yuan, X., Ni, J., Kind, R., Mechie, J. & Sandvol, E., 1997. Lithospheric and upper mantle structure of southern Tibet from a seismological passive source experiment, *J. geophys. Res.,* **102,** 27 491–27 500.

Zhu, L. & Kanamori, H., 2000. Moho depth variation in Southern California from teleseismic receiver functions, *J. geophys. Res.,* **105,** 2969–2980.

APPENDIX A: 5 STATION-DEPENDENT CRUSTAL MODELS

From the waveforms of the *P* and *S* waves arriving at the individual stations, crustal models have been determined using the approach of Kind *et al.* (1995) and a method modified from Zhu & Kanamori (2000). Table A1 gives the Moho depths derived as well as the mean crustal velocity values. The last three columns show the traveltimes of *P* and *S* waves through the top 71 km assuming vertical incidence. The resulting *P*–*S* delays at different stations differ by up to 1.8 s, emphasizing the need for crustal traveltimes.

APPENDIX B: RELIABILITY

Fig. B1 shows the beam coverage in four layers at depths between 300 and 660 km. The volcanic regions are marked by crosses and the hit counts for both areas with anomalies in the 410 km discontinuity exceed 40 per 10 km × 10 km bin. Due to the increasing size of the 1 s isochrons with depth, in general the coverage is better for greater depths.
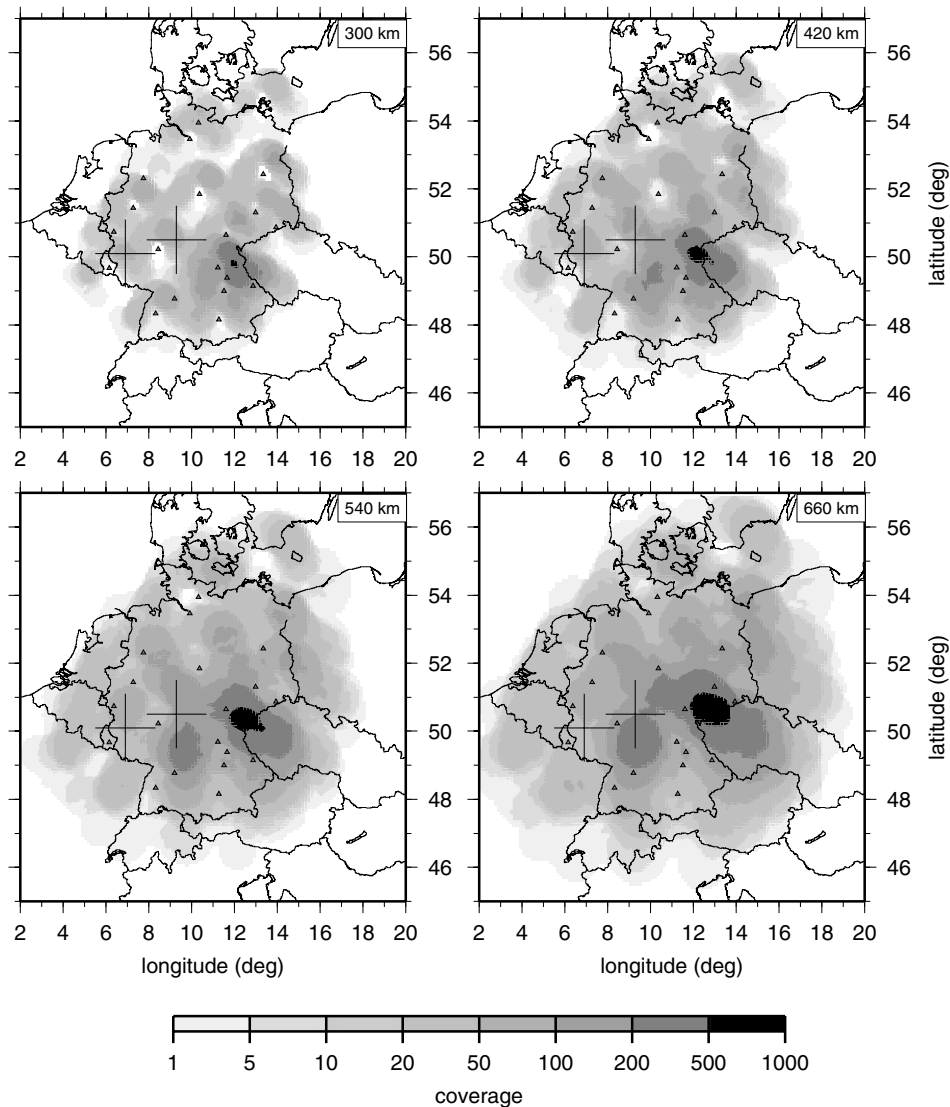

Figure B1. Hit coverage in 10 km × 10 km bins at 300, 420, 540 and 660 km depth. Rays have been widened to 1 s isochron beams. The Eifel region (as imaged in Fig. 12) and the Vogelsberg are marked by crosses. Note that both regions are well covered at the depths shown, with more than 40 beams contributing to each 10 km × 10 km bin.

Table A1. Crustal models for the stations used.

Station	Moho depth (km)	$\bar{v}_p$ crust (km s^{-1})	$\bar{v}_s$	t_p top 71 km (s)	t_s	t_{p-s}
BFO	26	5.60	3.21	9.7	17.1	7.4
BRG	30	5.83	3.31	9.8	17.4	7.6
BRNL	32.5	5.98	3.42	10.2	18.1	7.9
BSEG	28	6.06	3.40	10.4	19.2	8.8
BUG	35	5.73	3.29	10.3	18.6	8.3
CLL	28.5	6.16	3.48	10.0	17.4	7.5
CLZ	32	5.82	3.34	10.3	18.3	7.9
FUR	32	5.27	3.02	9.8	17.8	8.0
GRA1	27.5	5.49	3.15	10.4	18.3	8.0
GRB1	27.5	5.72	3.28	10.0	17.9	7.9
GRC1	27.5	5.58	3.19	10.1	17.6	7.6
GSH	29	5.62	3.22	9.4	17.0	7.6
HAM	32	5.22	2.98	11.1	19.5	8.4
IBBN	30	5.59	3.21	10.5	18.5	8.0
MOX	27	5.78	3.29	10.2	17.9	7.8
RGN	36.5	5.65	3.24	10.8	19.0	8.2
STU	26	5.95	3.37	9.7	17.0	7.3
TNS	27	5.71	3.24	9.3	16.3	7.0
WET	32	5.83	3.31	10.2	18.2	8.0
WLF	29	5.67	3.25	9.3	17.0	7.7